Chinese Journal of Catalysis 43 (2022) 130–138

available at www.sciencedirect.com

ScienceDirect

journal homepage: www.sciencedirect.com/journal/chinese-journal-of-catalysis

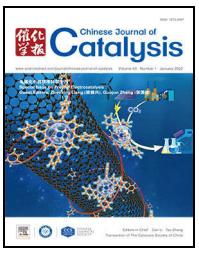

Article

Improved kinetics of OER on Ru-Pb binary electrocatalyst by decoupling proton-electron transfer

Rui Huang †, Yunzhou Wen †, Huisheng Peng, Bo Zhang *

State Key Laboratory of Molecular Engineering of Polymers, Department of Macromolecular Science, Fudan University, Shanghai 200438, China

ARTICLE INFO

Article history:
Received 28 May 2021
Accepted 2 June 2021
Available online 15 November 2021

Keywords:
Electrocatalysis
Acidic oxygen evolution reaction
Ruthenium oxide
In situ Raman
Proton-coupled electron transfer

ABSTRACT

The acidic oxygen evolution reaction (OER) is central to water electrolysis using proton-exchange membranes. However, even as benchmark catalysts in the acidic OER, Ru-based catalysts still suffer from sluggish kinetics owing to the scaling relationship that arises from the traditional concerted proton-electron transfer (CPET) process. Motivated by the knowledge that a charged surface may be favorable for accelerating the OER kinetics, we posited the incorporation of elements with pseudocapacitive properties into Ru-based catalysts. Herein, we report a $RuPbO_x$ electrocatalyst for efficient and stable water oxidation in acid with a low overpotential of 191 mV to reach 10 mA cm^{-2} and a low Tafel slope of 39 mV dec^{-1}. The combination of electrochemical analysis, X-ray photoelectron spectroscopy, and *in situ* Raman spectroscopy demonstrated that the improved OER kinetics was associated with the formation of superoxide precursors on the strongly charged surface after Pb incorporation, indicating a non-concerted proton-electron transfer mechanism for the OER on $RuPbO_x$.

1. Introduction

The oxygen evolution reaction (OER) is crucial for achieving a renewable energy cycle [1,2]. To achieve wide application of proton exchange membrane (PEM) electrolysis for hydrogen production, OER electrocatalysts that are active in acidic environments are urgently required [3–5]. Therefore, the design of highly efficient and durable OER catalysts and understanding the interfacial process remains an unmet challenge [6].

However, the harsh corrosive conditions of the OER limit acidic OER catalysts to ruthenium and iridium oxides [6–8], while the scarcity of Ir inhibits its large-scale application. Owing to their relative abundance, high OER activity, and corrosion resistance, Ru-based catalysts are the optimal alternative to Ir-based catalysts [9]. Unfortunately, a considerable overpotential is added to the actual process due to the complex and multiple steps in the OER. Thus, even as benchmark catalysts, Ru oxide catalysts still suffer from sluggish kinetics [10].

RuO_2 is generally considered to undergo a concerted proton-electron transfer (CPET) process during the OER, in which the proton(s) and electron(s) are transferred synchronously at each step. Therefore, the OER activity is limited by the scaling relationship that arises from CPET [11]. Prior studies suggest that involving a non-concerted proton-electron transfer pathway can break the scaling relationship and improve the OER performance in alkaline electrolytes [11,12]. Highly alkaline

* Corresponding author. Tel: +86-21-31242803; E-mail: bozhang@fudan.edu.cn
† Contributed equally to this work.
This work was supported by the National Natural Science Foundation of China (21875042, 21634003, 51573027), Ministry of Science and Technology of the People's Republic of China (2016YFA0203302), Shanghai Municipal Committee of Science and Technology (18QA140080, 16JC1400702) and the Program for Eastern Scholars at Shanghai Institutions.
DOI: 10.1016/S1872-2067(21)63856-1 | http://www.sciencedirect.com/journal/chinese-journal-of-catalysis | Chin. J. Catal., Vol. 43, No. 1, January 2022

environments facilitate the deprotonation process and form charged species (e.g., O^- and O_2^-), thereby decoupling proton and electron transfer [13–15]. Compared with alkaline conditions, it is difficult to decouple H^+ and e^- in the acidic OER because of the proton-rich environment. Therefore, most studies on Ru-based catalysts in the acidic OER did not achieve non-concerted proton-electron transfer steps [6,16,17]. To trigger the non-concerted proton-electron transfer process, modulating the charging state of the catalyst surface may be a promising strategy, by which deprotonation might be facilitated and the charged species can be stabilized under acidic conditions [18].

Motivated by the excellent pseudocapacitive properties and stability of lead and Pb oxides in acid [19,20], we posit that incorporating Pb into the Ru oxide lattice could alter the charging capability of the catalyst surface, thereby facilitating the formation of charged species to promote the non-concerted proton-electron transfer mechanism in order to enhance the OER performance.

In this study, a Ru-Pb binary oxide ($RuPbO_x$) electrocatalyst with homogeneous atomic dispersion is synthesized for the acidic OER. The catalyst affords a low overpotential of 191 mV to reach 10 mA cm^{-2} and a low Tafel slope of 39 mV dec^{-1}, which is lower than that of commercial nano-RuO_2. Electrochemical analysis and *in situ* Raman spectroscopy show that doping with Pb atoms changes the surface state of the pre-OER catalysts, enhances the charge capacity of the catalysts, and triggers the non-concerted proton-electron transfer mechanism to improve the OER performance.

2. Experimental

2.1. Materials

Ruthenium chloride hydrate ($RuCl_3{\cdot}xH_2O$), ruthenium oxide (RuO_2), carbon black (Vulcan XC-72), and Nafion® (5 wt% in a mixture of lower aliphatic alcohols and water) were purchased from Sigma-Aldrich. Lead acetate trihydrate ($Pb(Ac)_2{\cdot}3H_2O$) was purchased from Adamas-beta. Pt/C (40%) was obtained from Johnson Matthey. *N*,*N*-dimethylformamide (DMF), ethanol, isopropanol, and acetone were purchased from Sinopharm Reagent. $H_2{}^{18}O$ (99%) was purchased from Nukem Isotope. D_2O (99.9%) and D_2SO_4 (99.5%) were purchased from Cambridge Isotope. TGP-H-060 carbon paper (CP) was purchased from Toray. Freudenberg H23C9 gas diffusion layers were purchased from Fuel Cell Store. All the chemicals were used without further purification.

2.2. Synthesis of materials

A series of $RuPbO_x$ catalysts was synthesized by modifying a previously reported sol-gel method [21]. The typical procedure for $RuPbO_x$ synthesis is as follows: 0.75 mmol $RuCl_3{\cdot}xH_2O$ and 0.15 mmol $Pb(Ac)_2{\cdot}3H_2O$ were first dissolved in 3 mL DMF. The vessel with the solution was sealed and chilled in a refrigerator for 2 h, after which a clean stirring bar was placed into the solution. H_2O (0.2 mL) and propylene oxide (0.5 mL) were simultaneously dropped into the solution under stirring. The container was sealed and the mixture was aged for 12 h. Thereafter, the reaction was quenched by adding acetone, and the precipitates were immersed in acetone for 1 d, followed by centrifugation and washing with acetone three times to thoroughly remove propylene oxide and DMF. The as-prepared powder was dried under vacuum conditions. Afterward, the black powder was annealed in a tube furnace at 500 °C in air for 1 h at a ramp rate of 2 °C min^{-1}. Catalysts with different Ru:Pb ratios were synthesized using the same procedure as that for $RuPbO_x$. The total amount of metal salt precursors was kept at 0.9 mmol, and the ratio of the different precursors was varied.

2.3. Characterizations of catalysts

High-resolution transmission electron microscopy (HR-TEM) images and corresponding energy-dispersive X-ray spectroscopy (EDX) elemental maps were obtained using a JEOL-2100F TEM equipped with an Oxford energy dispersive spectrometer. Powder X-ray diffraction (PXRD) patterns were obtained using a Bruker D8 Advance diffractometer equipped with a Cu-K_α X-ray source. X-ray photoelectron spectroscopy (XPS) measurements were conducted on a Thermo Scientific K-alpha X-ray photoelectron spectrometer with a monochromatic Al-K_α X-ray source (1486.6 eV). The XPS data were further analyzed using CasaXPS software. Owing to the overlap of the C 1*s* and Ru 3*d* peaks, the binding energy was calibrated relative to the C-F_2 peaks from the Nafion® ionomer (290.8 eV) [22,23]. The details of X-ray absorption spectroscopy (XAS) measurements and analysis are provided in the Supporting Information (SI) and Supplementary Note 2.

2.4. Electrochemical measurements

Electrochemical measurements were performed in a three-electrode system using a potentiostat (Metrohm Autolab M204), with a saturated Hg/Hg_2SO_4 electrode (MSE, E^0 = 0.652 V *vs.* RHE at 25 °C) as the reference electrode and platinum foil as the counter electrode. To prepare the catalyst film on glassy carbon rotating disk electrodes (GCE, 3 mm in diameter), 5 mg of catalyst and 2 mg of carbon black were dispersed in 980 μL of a mixture of water and ethanol (5:1, *v*/*v*), after which 20 μL of 5 wt% Nafion® ionomer solution was added. The suspension was immersed in an ultrasonic bath for at least 60 min to obtain a homogeneous ink. Thereafter, 4.5 μL of the catalyst ink was carefully deposited onto the GCE (the loading mass was 0.32 mg cm^{-2}). Detailed electrochemical protocols are provided in the SI.

2.5. In situ Raman measurements

In situ electrochemical Raman spectroscopy measurements were carried out on a Renishaw In Via Qontor Raman spectrometer equipped with a 50× objective and 300 mW 785 nm laser. A homemade polytetrafluoroethylene electrochemical cell was used for the *in situ* measurements. A saturated Ag/AgCl electrode was used as the reference electrode, and a Pt

wire was used as the counter electrode. The working electrodes were prepared by airbrushing the catalyst powder onto the CPs. *In situ* Raman spectra were collected in conjunction with linear sweep voltammetry (LSV) measurements. The applied potential was elevated from 0.9 to 1.5 V *vs*. RHE at a scan rate of 2 mV s^{-1}. Each spectrum was acquired under 1.2 mW laser illumination (1% laser power and 40% optical efficiency) for 10 s. During the *in situ* measurements, the LiveTrack module was used to ensure that the laser focused on the sample to relieve interference from the bubbles generated in the OER. The above measurements were carried out in ordinary 0.5 M H_2SO_4, D_2SO_4, and ^{18}O labeled H_2SO_4 solutions to verify the isotope effect of the OER intermediates.

3. Results and discussion

3.1. Material characterization

The as-prepared catalyst was first studied using TEM, which demonstrated that the synthesized Ru-Pb oxide catalysts had a particle size of *ca.* 10 nm (Fig. 1(a)). The HR-TEM images and the corresponding fast Fourier-transform (FFT, Fig. 1(b) and inset) pattern indicated that the catalysts possessed the rutile structure. The spacing of the (110) crystal plane increased slightly upon Pb doping. Because Pb ions (0.94 Å for Pb^{2+} and 0.77 Å for Pb^{4+}) have a larger radius than Ru^{4+} ions (0.62 Å) [24], these deviations are plausibly due to the incorporation of Pb ions into the RuO_2 lattice. The PXRD results confirmed successful doping with Pb. As shown in Fig. 1(c), all the XRD peaks of the catalysts matched well with those of rutile RuO_2 in the tetragonal system and P42/mnm space group, where the peaks were negatively shifted by ~0.1° upon Pb doping, while no peaks related to Pb compounds were observed, indicating that the Pb ions may be dispersed in the rutile matrix instead of forming other phases. High-angle annular dark-field scanning transmission electron microscopy (HAADF-STEM) and EDX were employed to analyze the elemental distribution of the as-prepared catalysts (Fig. 1(d)). The elemental maps (Figs. 1(e)–(g)) show that Ru, Pb, and O were uniformly distributed over the entire catalyst, indicating the successful preparation of $RuPbO_x$ catalysts. In addition, the EDX analysis indicated that the atomic ratio of Ru/Pb was 4.3:1 when the feed ratio was

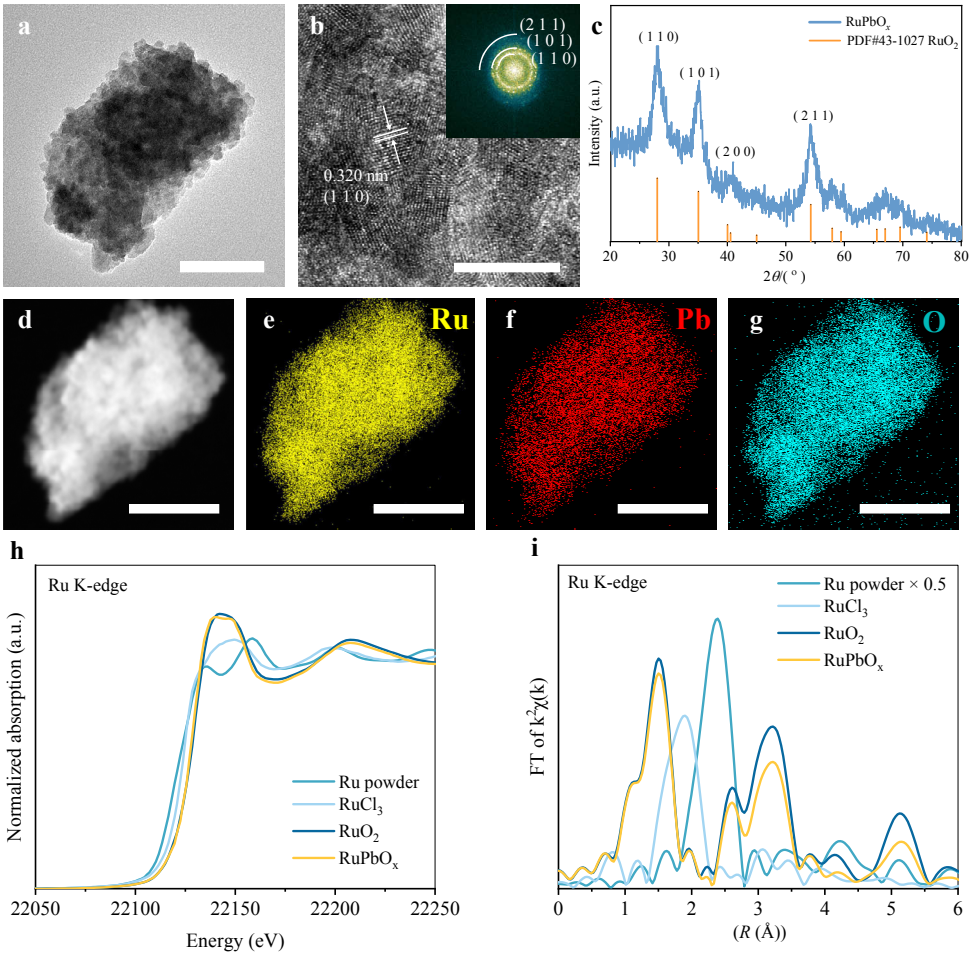

Fig. 1. Characterization of $RuPbO_x$ catalyst. (a) TEM image. Scale bar: 50 nm. (b) HR-TEM image. Inset: FFT pattern from the nanoparticle can be indexed to (110), (101), and (211) planes of rutile structure. Scale bar: 10 nm. (c) XRD patterns. (d–g) HADDF-STEM image and EDX element mappings. Scale bar: 50 nm. (h) Normalized Ru *K*-edge XANES spectra of $RuPbO_x$, Ru powder, $RuCl_3$, and commercial RuO_2. (i) Fourier-transform EXAFS profile of Ru *K*-edge for $RuPbO_x$, Ru powder, $RuCl_3$, and commercial RuO_2.

5:1.

XAS was further carried out to elucidate the electronic and atomic structures of $RuPbO_x$. Ru K-edge X-ray absorption near edge structure (XANES) analysis of the rutile-type $RuPbO_x$ showed that the absorption energy of $RuPbO_x$ is similar to that of $Ru(IV)O_2$, which is different from that of metallic Ru(0) powder and $Ru(III)Cl_3$, suggesting that the oxidation state of Ru in $RuPbO_x$ is close to +4 (Fig. 1(h)). Ru K-edge extended X-ray absorption fine structure (EXAFS) analysis was also applied to reveal the local structures of the Ru–O and Ru–Ru bonds. From the Fourier-transformed (FT) radial structure of the k^2-weighted EXAFS spectra (Fig. 1(i)), it was determined that the peak at 1.50 Å for RuO_2 is associated with Ru–O, while the peaks at 2.60 and 3.22 Å arise from the back scatterings of Ru–Ru in the second and third shell [25]. Compared with RuO_2, $RuPbO_x$ showed decreased intensity of the third shell Ru-Ru scattering, which could be ascribed to the decreased Ru-Ru coordination number after Pb doping. The detailed structural parameters of $RuPbO_x$ were obtained by fitting the EXAFS data (Supplementary Note 2). The best fit was obtained when the Ru-Pb scattering path was considered in the third-shell fitting (Fig. S1 and Table S1), indicating that Pb and Ru reached atomic-level blending in the rutile lattice.

3.2. Electrochemical performance

The OER performance of the catalysts in 0.5 M H_2SO_4 was evaluated by linear sweep voltammetry (LSV) (Fig. 2(a) and Table S2). After incorporating Pb atoms, the OER activity was enhanced to various extents compared to that of commercial nano-RuO_2 (Fig. S2), where the best performing catalyst was $Ru_5Pb_1O_x$ (based on the feed ratio, denoted as $RuPbO_x$ in the

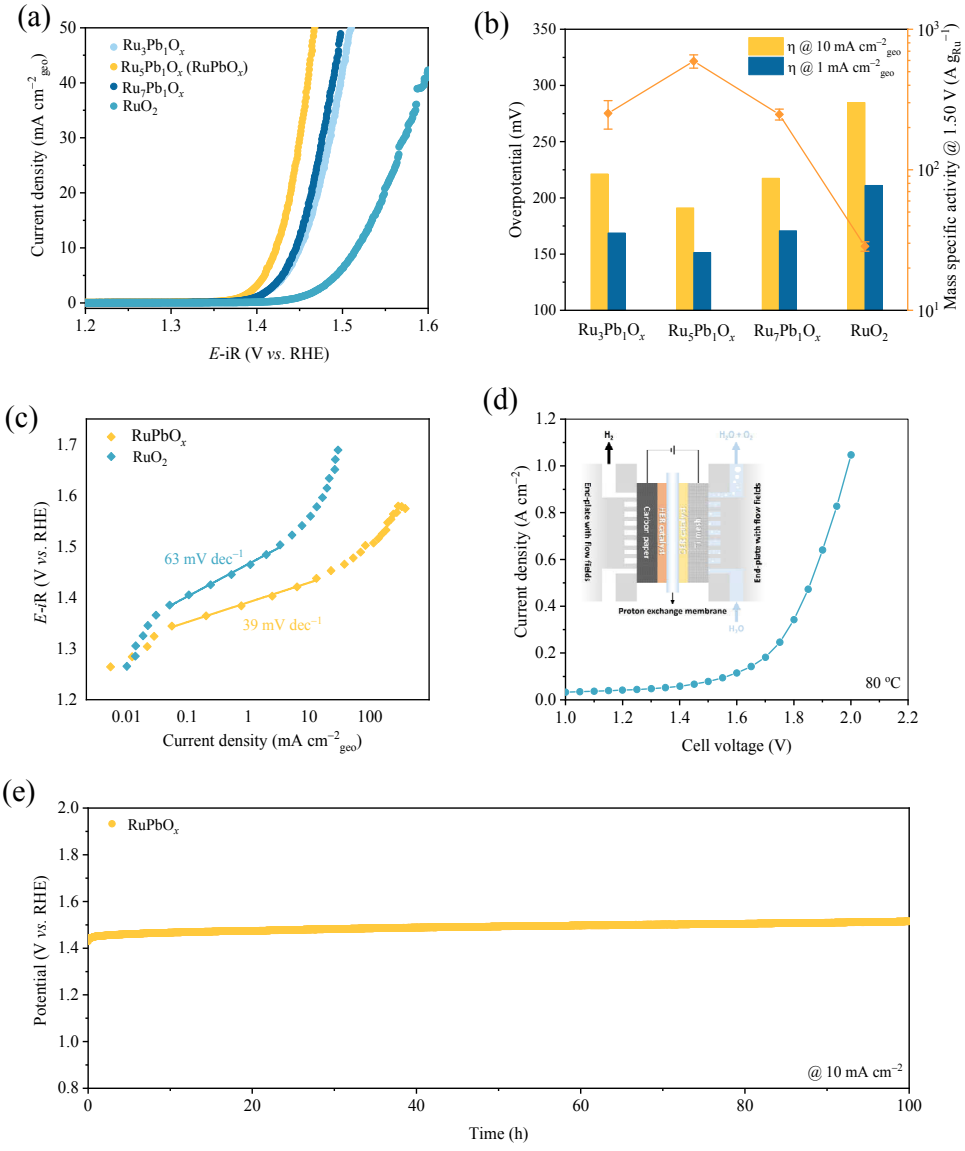

Fig. 2. Electrochemical performance. (a) OER polarization curves of different catalysts. The curves were 95% iR-compensated; (b) η_{10} and mass activities of different catalysts; (c) Steady-state Tafel plots for different catalysts; (d) Steady-state polarization curve of $RuPbO_x$ in PEM electrolyzer. Inset: schematic of PEM electrolyzer; (e) Chronopotentiometry stability test of $RuPbO_x$ at 10 mA cm^{-2}.

following discussion). The $RuPbO_x$ catalyst required an overpotential of only 191±3 mV to reach 10 mA cm^{-2} (η_{10}), which is a 94 mV improvement compared to that of RuO_2. The mass-specific activity of $RuPbO_x$ was 594 A g_{Ru}^{-1}, which is more than 20 times higher than that of RuO_2 (28 A g_{Ru}^{-1}), ranking it among the most active Ru-based catalysts in acid (Fig. 2(b) and Table S3). The turnover frequencies (TOFs) were also estimated on the basis of the total Ru loading (an underestimated method). The TOF of $RuPbO_x$ was approximately 0.143 s^{-1} at 1.50 V *vs.* RHE, which is 20 times higher than that of pristine RuO_2 (0.007 s^{-1}) (Fig. S3). To compare the intrinsic activity of $RuPbO_x$ and RuO_2, both the electrochemical surface area (ECSA) and Brunauer-Emmett-Teller (BET) surface areas were used to normalize the OER current (Supplementary Note 1, Figs. S4–S7). $RuPbO_x$ afforded a higher OER current density than RuO_2 (Figs. S6–S7), indicating that the improved OER activity is not due to the increase in the surface area, but rather to the intrinsic activity of the active sites.

The kinetic profiles of $RuPbO_x$ and RuO_2 were studied using electrochemical impedance spectroscopy (EIS) and steady-state Tafel measurements. EIS anlaysis showed that $RuPbO_x$ had a smaller charge-transfer resistance than RuO_2 (Figs. S8 and S9), while the effective surface double-layer capacitance ($C_{dl,eff}$) of $RuPbO_x$ was higher than that of RuO_2 (Table S4), suggesting faster OER kinetics on $RuPbO_x$ and a stronger surface charging capability. In the steady-state Tafel measurements, both catalysts exhibited approximate two-step Tafel behavior. At high overpotentials, the Tafel slope for both catalysts was ~120 mV dec^{-1}, which can be attributed to the decomposition of H_2O ($M + H_2O \rightarrow M\text{-}OH + H^+ + e^-$) as the rate-determining step [26,27]. In the low overpotential region, pristine RuO_2 demonstrated a Tafel slope of 63 mV dec^{-1}, which is close to previously reported values [28–31]. This value is believed to be associated with the deprotonation of *OH ($M\text{-}OH \rightarrow M\text{-}O + H^+ + e^-$), as the rate-limiting step. In contrast, the Tafel slope was 39 mV dec^{-1} for $RuPbO_x$, which not only indicates faster kinetics on the Pb-doped catalyst, but also suggests a change in the rate-determining step. According to the previous microkinetic analysis, the Tafel slope of ~40 mV dec^{-1} may be associated with the decoupled proton-electron transfer step as the rate-determining step [26]. This is discussed in detail later.

The OER stability of $RuPbO_x$ was then evaluated using chronopotentiometry at 10 mA cm^{-2} (Fig. 2(e)). The overpotential increased by only 85 mV for this new catalyst during 100 h of continuous electrolysis, which is superior to the performance of other doped Ru-based electrocatalysts [30,32,33]. To further verify the electrochemical performance of $RuPbO_x$ in practical systems, the catalyst was utilized in a 5 cm^2 PEM electrolyzer for water electrolysis under industrial conditions (80 °C) (Fig. 2(d)). The cell only required 2 V (without any compensation) to reach an electrolysis current density of 1 A cm^{-2}. The above results further validated the superior OER activity and stability of $RuPbO_x$.

3.3. Analysis of surface chemical state of $RuPbO_x$

To investigate the origin of the high activity of $RuPbO_x$, combined cyclic voltammetry (CV), pulse voltammetry (PV), and XPS analyses were used to study the surface chemical states of the catalysts. Over the potential range of 0–1.5 V *vs.* RHE, $RuPbO_x$ exhibited capacitive behavior and two redox reaction peaks in the CV cycle (Fig. 3(a)). The first peak in the region of 0.5–0.8

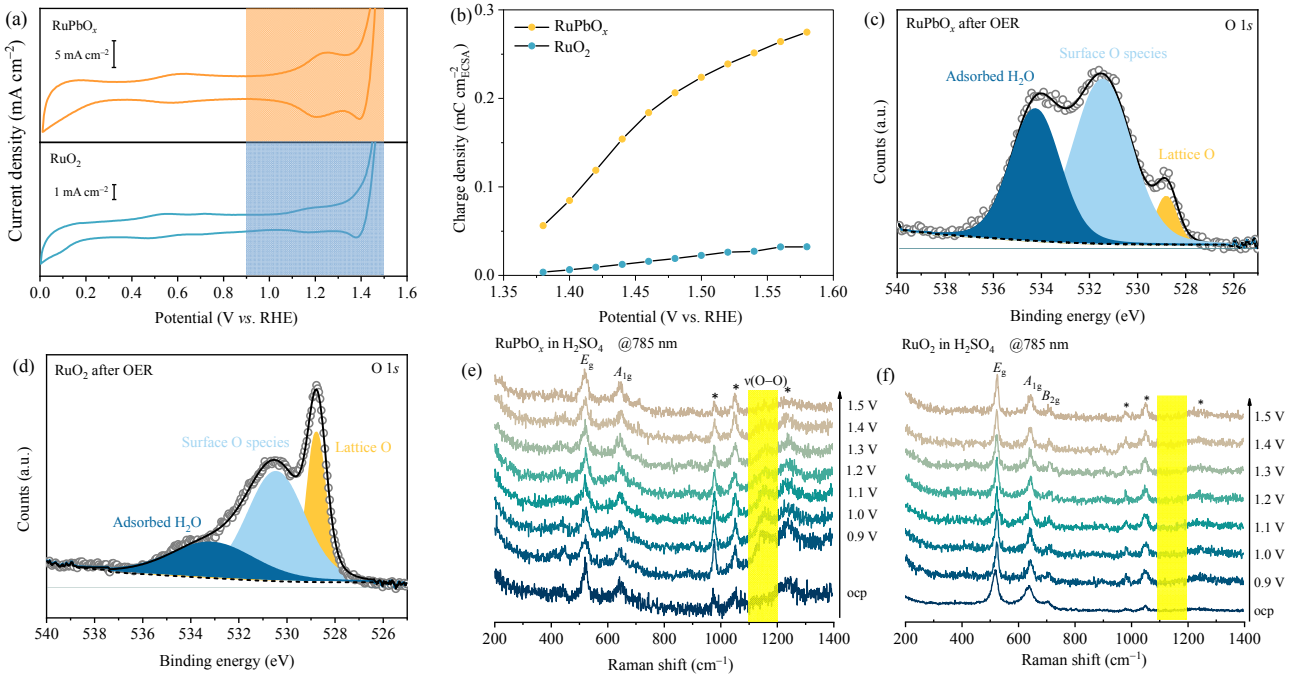

Fig. 3. Surface chemical state of $RuPbO_x$. (a) Cyclic voltammogram of $RuPbO_x$ in the range of 0–1.5 V *vs.* RHE at 200 mV s^{-1} scan rate; (b) Relationship between total charge and applied potential of different catalysts, measured by pulse voltammetry; (c,d) Fitted O 1*s* spectra for $RuPbO_x$ and RuO_2 after OER. The fits are described in the text; (e,f) *In situ* EC-Raman spectra of $RuPbO_x$ and RuO_2. * Peaks of H_2SO_4 electrolyte and substrate. The yellow region in (e) represents the superoxide species.

V originates from the oxidation of Ru^{3+} to Ru^{4+}, and the second peak at 1.1–1.4 V, before the OER onset, is assigned to surface charging and evolution of the chemical state of the catalyst [34,35]. Compared to RuO_2, $RuPbO_x$ exhibited a more prominent redox profile, indicating that the surface of $RuPbO_x$ was strongly charged and was oxidized before the OER onset.

Such pseudocapacitive charging effects can also be probed by PV (Fig. 3(b) and Fig. S10). The total charge stored on the catalyst surfaces (the charge density was normalized by the ECSA to eliminate the surface area effect) was measured by integrating the cathodic pulse current (Fig. S10). The $RuPbO_x$ catalyst demonstrated 8–15 times stronger surface charging than the pristine catalyst within the OER potential window. It has been pointed out that for Ru- (or Ir-) based materials, the OER rate is directly associated with this pseudocapacitive charging effect [18]. The catalyst surface can store charge through surface deprotonation. In $RuPbO_x$, this surface charging process may lead to the formation of a highly OER active surface before the OER, and some charged species may be stabilized on the catalyst surface and serve as reaction precursors. These charged surface species favor the non-concerted proton-electron transfer process [13].

The surface chemical environment of the post-OER catalysts was then examined using O 1*s* XPS (Figs. 3(c) and 3(d)). Three different oxygen species were resolved through deconvolution of the peaks of both $RuPbO_x$ and RuO_2 (Table S5). The peak at ~534.2 eV is assigned to adsorbed water, whereas the peaks at 531.4 and 528.8 eV are related to hydroxyl groups and lattice oxygen, respectively [36]. Compared with RuO_2, $RuPbO_x$ contained a larger proportion of adsorbed water and surface O species, suggesting that more active oxygen species were terminated on the catalyst surface, with fewer less-reactive divalent surface oxygen species [37].

3.4. *In situ Raman spectroscopy*

To further understand the evolution of the surface species of $RuPbO_x$ during the OER process, *in situ* electrochemical Raman spectroscopy (EC-Raman) was performed. Figs. 3(e) and 3(f) show the *in situ* Raman spectra of $RuPbO_x$ and RuO_2. Two major Raman features, located at *ca.* 528 and 644 cm^{-1}, were observed for both $RuPbO_x$ and RuO_2, which can be assigned to the E_g and A_{1g} modes in the rutile-type structure, respectively [38]. The B_{2g} mode (716 cm^{-1}, which originated from the Ru-O stretching vibration in the lattice) was faint for $RuPbO_x$, indicating that the surface microstructure of $RuPbO_x$ is different from that of RuO_2, which is consistent with the XPS signals of weak lattice O in $RuPbO_x$. The peaks at 800–1100 cm^{-1} are from the electrolyte (Fig. S11) [39].

$RuPbO_x$ showed a distinct Raman peak at ~1158 cm^{-1}, the intensity of which changed obviously as the potential increased from 0.9 to 1.5 V *vs*. RHE. In contrast, this Raman peak was not detected for RuO_2 (Fig. 3(f)). Deuterium isotopic substitution measurements showed that this peak did not exhibit discernible shifts, whereas in the $H_2S^{18}O_4$ electrolyte, the peak shifted to lower wavenumber (approximately 1148 cm^{-1}) (Fig. S12). The above results confirmed that the intermediates with signals around 1158 cm^{-1} are oxygen-related species. According to previous literature, this peak could be assigned to the O-O stretching vibration of the superoxide ion (O_2^-) [13,40–43]. The presence of charged superoxide species demonstrates that the catalyst surface was pre-oxidized to a highly active state before the OER. As the applied potential increased, the superoxide species decomposed and released O_2.

3.5. *Non-concerted proton-electron transfer step in OER*

The observation of charged superoxide OER precursors in the Raman studies suggest that the OER process on the $RuPbO_x$ surface may proceed *via* a non-concerted proton-electron transfer pathway, which is distinct from that on RuO_2. We further investigated the pH-dependence of the OER activity (Fig. S13). At a given overpotential (η = 300 mV), the OER current of $RuPbO_x$ increased significantly as the pH decreased (Fig. 4(a)), demonstrating a reaction order $(\partial \log(i)/\partial \mathrm{pH})_E$ of −0.87. The Tafel slope also decreased with decreasing pH (Fig. 4(b)). The pH-dependence of the OER activity on the RHE scale indicated non-concerted proton-electron transfer steps during the OER [12]. In contrast, the OER activity of RuO_2 showed a weak dependence on the pH, which is consistent with classical CPET steps [8].

Based on the above results, we propose a possible mechanism for the electrocatalytic OER on $RuPbO_x$, which differs from the concerted proton-electron transfer mechanism that only considers uncharged adsorbates (or adsorbates with all equal charges) [12,13].

Non-concerted proton-electron OER mechanisms:

$$M + H_2O \rightarrow M\text{–}OH + H^+ + e^- \quad (1)$$

$$M\text{–}OH \rightarrow M\text{–}O + H^+ + e^- \quad (2)$$

$$M\text{–}O + H_2O \rightarrow M\text{–}OOH + H^+ + e^- \quad (3)$$

$$M\text{–}OOH + H_2O \rightarrow M\text{–}OO^- + H_3O^+ \quad (4)$$

$$M\text{–}OO^- \rightarrow M + O_2 + e^- \quad (5)$$

Eqs. (4) and (5) demonstrate that in this mechanism, decoupling of the proton and electron transfer processes (Fig. 4(c)), in which the M-OOH species are first deprotonated and form superoxide species M-OO^-, is followed by an electron transfer step and release of O_2. Previous microkinetic analysis of this non-concerted mechanism gave a theoretical Tafel slope of 40 mV dec^{-1} at low overpotential [26], where the present experimental value is very close to the theoretical value.

This mechanism is achieved by atomic-scale doping of Pb in the $RuPbO_x$ catalyst. The incorporation of Pb modified the local microstructure of rutile Ru oxide and increased the pseudocapacitive charging capability of the catalyst surface. This strongly charged surface promotes the deprotonation of surface oxo-species and stabilizes the charged OER precursors, such as superoxide ions (O_2^-), resulting in a decoupled proton-electron transfer process.

4. Conclusions

A $RuPbO_x$ electrocatalyst was developed for the acidic OER using a modified sol-gel method. The catalyst achieved a low overpotential of 191 mV to reach 10 mA cm^{-2} and a low Tafel

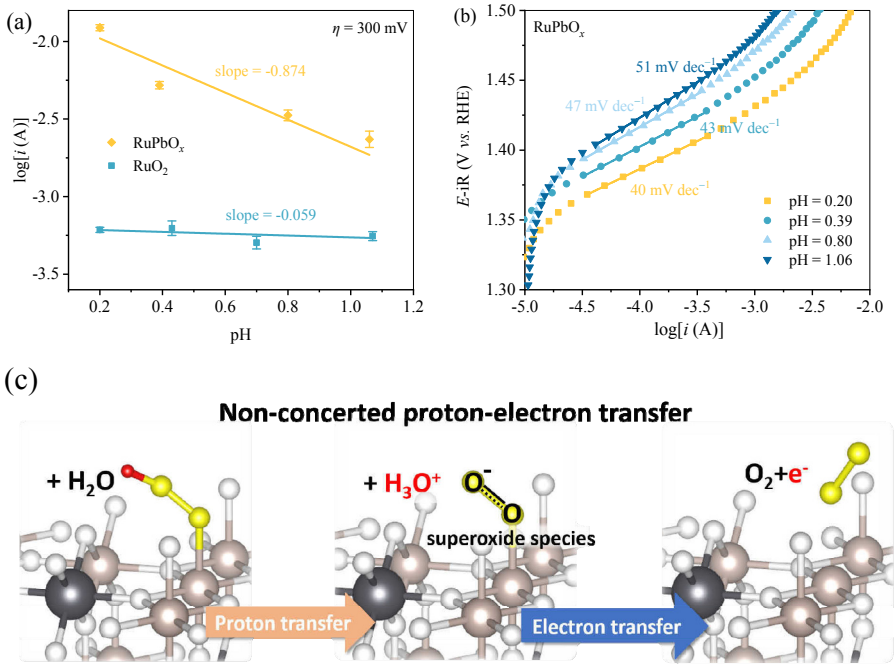

Fig. 4. Non-concerted proton-electron transfer steps on $RuPbO_x$. (a) pH-dependent OER activity of $RuPbO_x$ and RuO_2 at η = 300 mV; (b) pH-Dependence of Tafel slope of $RuPbO_x$; (c) Schematic of the non-concerted proton-electron transfer mechanism. Brown balls: Ru, black balls: Pb, white balls: O, red ball: H. The active oxygen species are marked with yellow.

slope of 39 mV dec^{-1}, where the slope is superior to that of commercial nano-RuO_2. The combination of electrochemical analysis, XPS, and *in situ* Raman spectroscopy demonstrated that the improved OER kinetics is associated with the formation of superoxide precursors on the strongly charged surface after Pb incorporation, indicating a non-concerted proton-electron transfer mechanism for the OER on $RuPbO_x$. These results pave the way for the design of efficient and durable electrocatalysts for the OER and other electrocatalytic applications.

Electronic supporting information

Supporting information is available in the online version of this article.

References

[1] C. Spori, J. T. H. Kwan, A. Bonakdarpour, D. P. Wilkinson, P. Strasser, *Angew. Chem. Int. Ed.*, **2017**, 56, 5994–6021.
[2] Z. W. Seh, J. Kibsgaard, C. F. Dickens, I. Chorkendorff, J. K. Nørskov, T. F. Jaramillo, *Science*, **2017**, 355, eaad4998.
[3] K. Sardar, E. Petrucco, C. I. Hiley, J. D. Sharman, P. P. Wells, A. E. Russell, R. J. Kashtiban, J. Sloan, R. I. Walton, *Angew. Chem. Int. Ed.*, **2014**, 53, 10960–10964.
[4] Y. Wen, P. Chen, L. Wang, S. Li, Z. Wang, J. Abed, X. Mao, Y. Min, C. T. Dinh, P. Luna, R. Huang, L. Zhang, L. Wang, L. Wang, R. J. Nielsen, H. Li, T. Zhuang, C. Ke, O. Voznyy, Y. Hu, Y. Li, W. A. Goddard Iii, B. Zhang, H. Peng, E. H. Sargent, *J. Am. Chem. Soc.*, **2021**, 143, 6482–6490.
[5] Y. Liu, X. Liang, H. Chen, R. Gao, L. Shi, L. Yang, X. Zou, *Chin. J. Catal.*, **2021**, 42, 1054–1077.
[6] L. C. Seitz, C. F. Dickens, K. Nishio, Y. Hikita, J. Montoya, A. Doyle, C. Kirk, A. Vojvodic, H. Y. Hwang, J. K. Norskov, T. F. Jaramillo, *Science*, **2016**, 353, 1011–1014.
[7] S. Kumari, B. P. Ajayi, B. Kumar, J. B. Jasinski, M. K. Sunkara, J. M. Spurgeon, *Energy Environ. Sci.*, **2017**, 10, 2432–2440.
[8] L. Giordano, B. Han, M. Risch, W. T. Hong, R. R. Rao, K. A. Stoerzinger, Y. Shao-Horn, *Catal. Today*, **2016**, 262, 2–10.
[9] Y. Yao, S. Hu, W. Chen, Z.-Q. Huang, W. Wei, T. Yao, R. Liu, K. Zang, X. Wang, G. Wu, W. Yuan, T. Yuan, B. Zhu, W. Liu, Z. Li, D. He, Z. Xue, Y. Wang, X. Zheng, J. Dong, C.-R. Chang, Y. Chen, X. Hong, J. Luo, S. Wei, W.-X. Li, P. Strasser, Y. Wu, Y. Li, *Nat. Catal.*, **2019**, 2, 304–313.
[10] H. Dau, C. Limberg, T. Reier, M. Risch, S. Roggan, P. Strasser, *ChemCatChem*, **2010**, 2, 724–761.
[11] M. T. M. Koper, *Chem. Sci.*, **2013**, 4, 2710–2723.
[12] A. Grimaud, O. Diaz-Morales, B. Han, W. T. Hong, Y. L. Lee, L. Giordano, K. A. Stoerzinger, M. T. M. Koper, Y. Shao-Horn, *Nat. Chem.*, **2017**, 9, 457–465.
[13] O. Diaz-Morales, D. Ferrus-Suspedra, M. T. M. Koper, *Chem. Sci.*, **2016**, 7, 2639–2645.
[14] Y. Matsumoto, H. Manabe, E. Sato, *J. Electrochem. Soc.*, **1980**, 127, 811–814.
[15] Y. Matsumoto, S. Yamada, T. Nishida, E. Sato, *J. Electrochem. Soc.*, **1980**, 127, 2360–2364.
[16] Y. Hu, X. Luo, G. Wu, T. Chao, Z. Li, Y. Qu, H. Li, Y. Wu, B. Jiang, X. Hong, *ACS Appl. Mater. Interfaces*, **2019**, 11, 42298–42304.
[17] J. Yi, W. H. Lee, C. H. Choi, Y. Lee, K. S. Park, B. K. Min, Y. J. Hwang, H.-S. Oh, *Electrochem. Commun.*, **2019**, 104, 106469.
[18] H. N. Nong, L. J. Falling, A. Bergmann, M. Klingenhof, H. P. Tran, C. Spöri, R. Mom, J. Timoshenko, G. Zichittella, A. Knop-Gericke, S. Piccinin, J. Pérez-Ramírez, B. R. Cuenya, R. Schlögl, P. Strasser, D. Teschner, T. E. Jones, *Nature*, **2020**, 587, 408–413.

Graphical Abstract

Chin. J. Catal., 2022, 43: 130–138 doi: 10.1016/S1872-2067(21)63856-1

Improved kinetics of OER on Ru-Pb binary electrocatalyst by decoupling proton-electron transfer

Rui Huang, Yunzhou Wen, Huisheng Peng, Bo Zhang *
Fudan University

A $RuPbO_x$ electrocatalyst was developed for the acidic OER. Pb incorporation enhanced the charging capability of the catalyst surface and improved the OER kinetics through a non-concerted proton-electron pathway.

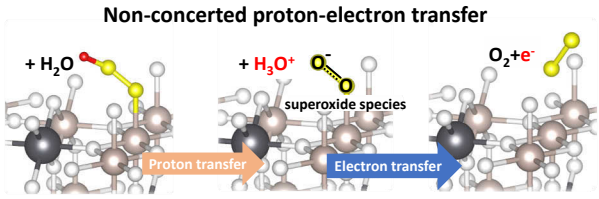

[19] X. Li, D. Pletcher, F. C. Walsh, *Chem. Soc. Rev.*, **2011**, 40, 3879–3894.
[20] Y. Yao, G. Teng, Y. Yang, C. Huang, B. Liu, L. Guo, *Sep. Purif. Technol.*, **2019**, 211, 456–466.
[21] B. Zhang, X. Zheng, O. Voznyy, R. Comin, M. Bajdich, M. Garcia-Melchor, L. Han, J. Xu, M. Liu, L. Zheng, F. P. Garcia de Arquer, C. T. Dinh, F. Fan, M. Yuan, E. Yassitepe, N. Chen, T. Regier, P. Liu, Y. Li, P. De Luna, A. Janmohamed, H. L. Xin, H. Yang, A. Vojvodic, E. H. Sargent, *Science*, **2016**, 352, 333–337.
[22] C. Girardeaux, J.-J. Pireaux, *Surf. Sci. Spectra*, **1996**, 4, 138–141.
[23] M. Schulze, M. Lorenz, T. Kaz, *Surf. Interface Anal.*, **2002**, 34, 646–651.
[24] R. D. Shannon, *Acta Cryst. A*, **1976**, 32, 751–767.
[25] J. Kim, P. C. Shih, K. C. Tsao, Y. T. Pan, X. Yin, C. J. Sun, H. Yang, *J. Am. Chem. Soc.*, **2017**, 139, 12076–12083.
[26] T. Shinagawa, A. T. Garcia-Esparza, K. Takanabe, *Sci. Rep.*, **2015**, 5, 13801.
[27] J. Zhang, H. B. Tao, M. Kuang, H. B. Yang, W. Cai, Q. Yan, Q. Mao, B. Liu, *ACS Catal.*, **2020**, 10, 8597–8610.
[28] Y. H. Fang, Z. P. Liu, *J. Am. Chem. Soc.*, **2010**, 132, 18214–18222.
[29] P. Castelli, S. Trasatti, F. H. Pollak, W. E. O'Grady, *J. Electroanal. Chem. Interf. Electrochem.*, **1986**, 210, 189–194.
[30] Y. Lin, Z. Tian, L. Zhang, J. Ma, Z. Jiang, B. J. Deibert, R. Ge, L. Chen, *Nat. Commun.*, **2019**, 10, 162.
[31] R. R. Rao, M. J. Kolb, L. Giordano, A. F. Pedersen, Y. Katayama, J. Hwang, A. Mehta, H. You, J. R. Lunger, H. Zhou, N. B. Halck, T. Vegge, I. Chorkendorff, I. E. L. Stephens, Y. Shao-Horn, *Nat. Catal.*, **2020**, 3, 516–525.
[32] S. Chen, H. Huang, P. Jiang, K. Yang, J. Diao, S. Gong, S. Liu, M. Huang, H. Wang, Q. Chen, *ACS Catal.*, **2019**, 10, 1152–1160.
[33] J. Su, R. Ge, K. Jiang, Y. Dong, F. Hao, Z. Tian, G. Chen, L. Chen, *Adv. Mater.*, **2018**, 30, e1801351.
[34] S. H. Chang, N. Danilovic, K. C. Chang, R. Subbaraman, A. P. Paulikas, D. D. Fong, M. J. Highland, P. M. Baldo, V. R. Stamenkovic, J. W. Freeland, J. A. Eastman, N. M. Markovic, *Nat. Commun.*, **2014**, 5, 4191.
[35] M. E. G. Lyons, S. Floquet, *Phys. Chem. Chem. Phys.*, **2011**, 13, 5314–5335.
[36] T. Reier, D. Teschner, T. Lunkenbein, A. Bergmann, S. Selve, R. Kraehnert, R. Schlögl, P. Strasser, *J. Electrochem. Soc.*, **2014**, 161, F876–F882.
[37] T. Reier, Z. Pawolek, S. Cherevko, M. Bruns, T. Jones, D. Teschner, S. Selve, A. Bergmann, H. N. Nong, R. Schlogl, K. J. Mayrhofer, P. Strasser, *J. Am. Chem. Soc.*, **2015**, 137, 13031–13040.
[38] S. Y. Mar, C. S. Chen, Y. S. Huang, K. K. Tiong, *Appl. Surf. Sci.*, **1995**, 90, 497–504.
[39] H. C. Jo, K. M. Kim, H. Cheong, S.-H. Lee, S. K. Deb, *Electrochem. Solid-State Lett.*, **2005**, 8, E39–E41.
[40] J.-C. Dong, X.-G. Zhang, V. Briega-Martos, X. Jin, J. Yang, S. Chen, Z.-L. Yang, D.-Y. Wu, J. M. Feliu, C. T. Williams, Z.-Q. Tian, J.-F. Li, *Nat. Energy*, **2018**, 4, 60–67.
[41] H. Y. Wang, S. F. Hung, Y. Y. Hsu, L. Zhang, J. Miao, T. S. Chan, Q. Xiong, B. Liu, *J. Phys. Chem. Lett.*, **2016**, 7, 4847–4853.
[42] S. A. Hunter-Saphir, J. A. Creighton, *J. Raman Spectrosc.*, **1998**, 29, 417–419.
[43] J. Kim, A. A. Gewirth, *J. Phys. Chem. B*, **2006**, 110, 2565–2571.

解耦质子-电子传输促进Ru-Pb二元电催化剂上的OER动力学

黄 睿†, 温蕴周†, 彭慧胜, 张 波*
复旦大学高分子科学系, 聚合物分子工程国家重点实验室, 上海200438

摘要: 开发酸性条件下的析氧反应(OER)电催化剂是质子交换膜(PEM)电解水技术的核心问题. Ru基催化剂作为酸性OER中的基准催化剂, 其OER活性被传统的协同质子-电子转移过程带来的比例关系所限制, 仍然存在动力学迟缓的问题. 基于荷电表面可能有利于加速OER动力学的认识, 本文将具有赝电容性质的元素Pb加入Ru基催化剂中以提升OER活性. 本文采用一种改进的溶胶-凝胶法制备得到$RuPbO_x$电催化剂, 用于酸性条件下高效和稳定的水氧化. 高分辨透射电镜及X射线吸收谱结果表明, $RuPbO_x$催化剂为约10 nm颗粒, Ru、Pb和O原子均匀分布在催化剂中, 形成原子级的混合. 电化学测试结果表明, 该催化剂达到10 mA cm^{-2}的过电位仅需191 ± 3 mV, 相比于商业纳米RuO_2提升了94 mV. 该催化剂的质量比活性及转化频率(TOF)相较于RuO_2提高了20倍. 经过电化学活性面积(ECSA)归一化的OER电流也显著提升, 表明Pb掺杂后提高了催化剂的本征活性. Tafel动力学研究结果表明, $RuPbO_x$的Tafel斜率为39 mV dec^{-1}, 而RuO_2的为63 mV dec^{-1}, 表明

$RuPbO_x$与RuO_2决速步骤不同. 该$RuPbO_x$催化剂还表现出较好的稳定性, 在10 mA cm^{-2}电流密度下连续电解100 h后过电位仅提升85 mV. 将该催化剂应用在工业条件(80 °C)下的质子交换膜(PEM)电解装置中, 到达1 A cm^{-2}电流密度时全电池电压仅需2 V.

使用X射线光电子能谱(XPS)、电化学分析以及原位拉曼光谱研究了催化剂表面的化学状态. 脉冲伏安法研究表明, Pb掺杂后的催化剂具有更强的荷电能力. O 1*s* XPS结果表明, 反应后$RuPbO_x$表面被更多活性氧物种覆盖. 电化学原位拉曼光谱研究表明, 在约1158 cm^{-1}出现了超氧根物种的伸缩振动峰, 随着电势的增加, 超氧根物种逐渐消耗并释放出氧气. 基于以上实验结果认为, $RuPbO_x$催化剂在OER过程中可能经历了一个与RuO_2不同的非协同质子-电子传输路径. $RuPbO_x$的OER活性也表现出了pH相关性, 进一步证明了非协同质子-电子转移的发生. 原子级的Pb掺杂可以调控金红石氧化钌的局域微结构, 增加了催化剂表面的电容性荷电能力. 这种强荷电的表面可以促进含氧中间体的去质子化并稳定带电的OER前驱物(例如超氧根离子), 从而将质子-电子转移过程解耦, 打破比例关系的限制, 提升OER活性.

关键词: 电催化; 酸性析氧反应; 氧化钌; 原位拉曼; 质子-电子转移

收稿日期: 2021-05-28. 接受日期: 2021-06-02. 上网时间: 2021-11-15.

*通讯联系人. 电话: (021)31242803; 电子信箱: bozhang@fudan.edu.cn

†共同第一作者.

基金来源: 国家自然科学基金(21875042, 21634003, 51573027); 中华人民共和国科技部研发项目(2016YFA0203302); 上海市科技委(18QA140080, 16JC1400702); 上海市“东方学者”岗位计划.

本文的电子版全文由Elsevier出版社在ScienceDirect上出版(http://www.sciencedirect.com/journal/chinese-journal-of-catalysis).